Mammary Tumors in Sprague Dawley Rats Induced by ENU for Evaluating Terahertz Imaging of Breast Cancer

3

- Nagma Vohra, Tanny Chavez, Joel Rodriguez Troncoso, Narasimhan Rajaram, Jingxian
- 5 Wu,^a Patricia N. Coan,^c Todd A. Jackson,^c Keith Bailey,^d and Magda El-Shenawee^a
- 6 ^a University of Arkansas, Bell Engineering Center, Department of Electrical Engineering, Fayetteville, Arkansas, United States
- 8 b University of Arkansas, Bell Engineering Center, Department of Biomedical Engineering, Fayetteville, Arkansas,
 United States
- 10 °Oklahoma State University, Animal Resources Unit, Stillwater, Oklahoma, United States
 - ^d University of Illinois, Urbana-Champaign, Veterinary Diagnostic Laboratory, Urbana, Illinois, United States

11 12 13

- Abstract
- Purpose: The objective of this study is to quantitatively evaluate terahertz (THz) imaging for differentiating cancerous from non-cancerous tissues in mammary tumors developed in response to injection of ENU in Sprague Dawley rats.
- Approach: While previous studies have investigated the biology of mammary tumors of this model, the current work is the first study to employ an imaging modality to visualize these tumors. A pulsed THz imaging system is utilized to experimentally collect the time domain reflection signals from each pixel of the rat's excised tumor. A statistical segmentation algorithm based on the expectation maximization (EM) classification method is implemented to quantitatively assess the obtained THz images. The model classification of cancer is reported in terms of the receiver operating characteristic (ROC) curves and the areas under the curves.

22 23

24

25

26

27

- **Results:** The obtained low power microscopic images of 17 ENU-rat tumor sections exhibited the presence of healthy connective tissue adjacent to cancerous tissue. The results also demonstrated that high reflection THz signals were received from cancerous compared with non-cancerous tissues. Decent tumor classification was achieved using the EM method with values ranging from 83% to 96% in fresh tissues and 89% to 96% in formalin fixed paraffin embedded tissues.
- Conclusions: The proposed ENU breast tumor model of Sprague Dawley rats showed a potential to obtain cancerous tissues adjacent to healthy tissues like human breast tumors. The implemented EM classification algorithm quantitatively demonstrated the ability of THz imaging in differentiating cancerous from non-cancerous tissues.
- Keywords: Terahertz imaging, reflection mode, breast cancer, ENU-rat tumor induction, Sprague Dawley rats, microscopic imaging, expectation maximization classification method.

33 34

*Magda El-Shenawee, E-mail: magda@uark.edu

35

36

1 Introduction

- 37 Terahertz (THz) imaging has emerged as a potential clinical technology for noninvasive and
- 38 nonionizing evaluation of breast tumor margins [1-4]. Leveraging its sensitivity to water content,
- 39 THz imaging has been used to determine the differences between normal and diseased tissue in
- 40 several organs [5-9]. To establish the feasibility of THz imaging for imaging breast tumor margins,

we and others have shown the ability of THz imaging to distinguish between tumors and the surrounding fatty tissue in subcutaneous tumor xenograft models of breast cancer [10-13]. These tumor models are established from subcutaneous injections of immortalized cancer cells and result in the formation of distinct tumor cells and fatty tissue compartments. However, these tumors are nearly devoid of fibrous tissue and therefore do not adequately represent the complexity of human breast cancer. Recent work from our group demonstrated the first THz imaging study [14] in a transgenic mouse model of breast cancer (MMTV-PyMT), which has been used extensively as a preclinical model of breast cancer due to its similarities to the complexity and progression of human breast cancer [15, 16]. Despite the incredible tumor heterogeneity that was similar to what we have observed in our studies of human breast cancer [3, 17-20], there were appreciable differences in THz signal between different tumor compartments, such as fibrous, adipose (with and without tumor infiltration), tumor, and glandular secretions. However, the relative contributions of fatty and fibrous tissue to these tumors were still not reflective of human breast cancer [21]. Specifically, these transgenic tumors exhibit progressive degradation of the extracellular matrix with tumor progression, resulting in nearly 70-80% of the tumor being composed of adipose tissue at the time of tumor excision in our study. In our previous work [3], we reported tomographic images of freshly excised cancerous and healthy tissues obtained from patients and breast reduction surgeries, respectively. It is a continuous challenge, in cost and frequency, to acquire an adequate number of freshly excised human tumors that include normal tissue adjacent to cancerous tissue needed to assess the tumor margins. While no model can perfectly replicate human disease, our use of THz imaging and image analysis algorithms that leverage differences in the reflection signatures from different tissue compartments necessitate the use of a model that is a closer representation of the human breast tumors.

41

42

43

44

45

46

47

48

49

50

51

52

53

54

55

56

57

58

59

60

61

62

63

The development of carcinogen-induced mammary tumors in rodents has been used as a preclinical model, albeit not as extensively as transgenic or tumor xenograft models. Studies have shown that injection of N-ethyl-N-nitrosourea (ENU) results in reliable growth of benign and malignant mammary tumors [22-24]. These tumors have several similarities to human breast cancer, including elevated serum calcium and local invasion into the stroma and muscle. Rats were found to develop mammary tumors between 50- and 155-days post-injection [24]. As such, the ENU model of breast cancer has the potential to present tumors that are like human breast tumors in both complexity and composition (i.e. presence of cancerous adjacent to fatty and healthy connective tissues).

The objective of this study is to determine the ability of THz imaging to differentiate cancerous and non-cancerous tissue in mammary tumors that develop in response to injection of ENU in rats. While previous studies by others conducted investigations of mammary tumor biology in these models [25-27], this is the first study to employ an imaging modality to visualize these tumors. In addition to imaging cancer and non-cancer tissue within each tumor in both fresh and formalin-fixed paraffin-embedded forms (FFPE), we also report the results of a new classification analysis based on the expectation maximization technique [28] and a side-by-side comparison with xenograft and transgenic mice models. To ensure an objective comparison across all tumor models, our classification algorithm only considers two compartments— cancer and non-cancer.

This work is organized as follows: methodology describing the rodent injections, pulsed THz imaging system, pre-image preparation of fresh tumor tissue, and image segmentation based on the expectation maximization technique are discussed in Section 2, results of THz imaging of ENU-rat tumors, a comparison to other mice tumor models, and THz image analysis and

- classification are presented in Section 3, and conclusion and future work is discussed in Section 4.
- 87 The microscopic imaging and image analysis procedure is discussed in Appendix A.

2 Methodology

88

89

90

91

92

93

94

95

96

97

98

99

100

101

102

103

104

105

106

2.1 ENU Tumor Induction in Rats

All the rats handled in this work were injected with N-ethyl-N-nitrosourea (ENU) chemical solution at the Oklahoma State University. Two batches of ten 30-day old female Sprague Dawley rats were purchased from Charles River, Wilmington, MA, USA, and housed to acclimate for at least two days after arrival. The rats were kept two per cage in static filtered microisolator cages with corn cob bedding (Bed' OCobs, Maumee, OH, USA). Rats were fed rodent chow (Lab Diet 5001, St. Louis, MO, USA) and tap water ad libitum. The weight of the rats ranged between 150 and 186 grams. An amount of 15 mL of phosphate citrate buffer (Sigma-Aldrich, Milwaukee, WI, USA) was infused into the ipsopac containing the ENU solution (Sigma-Aldrich, Milwaukee, WI, USA). The rats were given 165 mg/kg of the ENU solution intraperitoneally in the lower right quadrant of the peritoneal cavity. All the animal procedures were performed in a chemical safety fume hood [29]. The cages were changed every four days, with the waste being handled as chemical hazardous for the first four days. Two weeks after inoculation, the rats were shipped to the University of Arkansas, where they were housed in the animal facility. The rats were maintained at standard 12-hour light/dark cycles with regular access to food and water. Tumors were excised between 9 and 21 weeks, with sizes ranging between 8 mm and 18 mm in diameter. The protocols for injecting rats with ENU chemical to produce mammary tumors were approved by the Institutional Animal Care and Use Committee (IACUC) of the Oklahoma State

University. Additionally, protocols for all rat experiments were approved by the Institutional
Animal Care & Use Committee (IACUC) of the University of Arkansas.

2.2 Pulsed Terahertz Imaging System

The diagram of the pulsed terahertz system utilized in this work is shown in Fig. 1. The terahertz emitter and receiver antennas are voltage biased bow-tie antennas on the GaAs substrate [20]. Fig. 1c shows the generated THz signal upon excitation with a 780 nm wavelength Ti: Sapphire laser beam. The Fourier transform of the time domain pulse gives the spectrum ranging from 0.1 THz to 4 THz, Fig. 1d. The generated THz pulse is directed onto the tissue sample, and the reflected signal is collected at the receiver antenna. For fresh tissue imaging, the specimen is placed between two polystyrene plates. The incident THz signal is directed on this polystyrene-tissue arrangement, and the reflected signal is recorded at the receiver antenna. In this case, two reflected pulses are received, one from the air-polystyrene interface and the second from the polystyrene-tissue

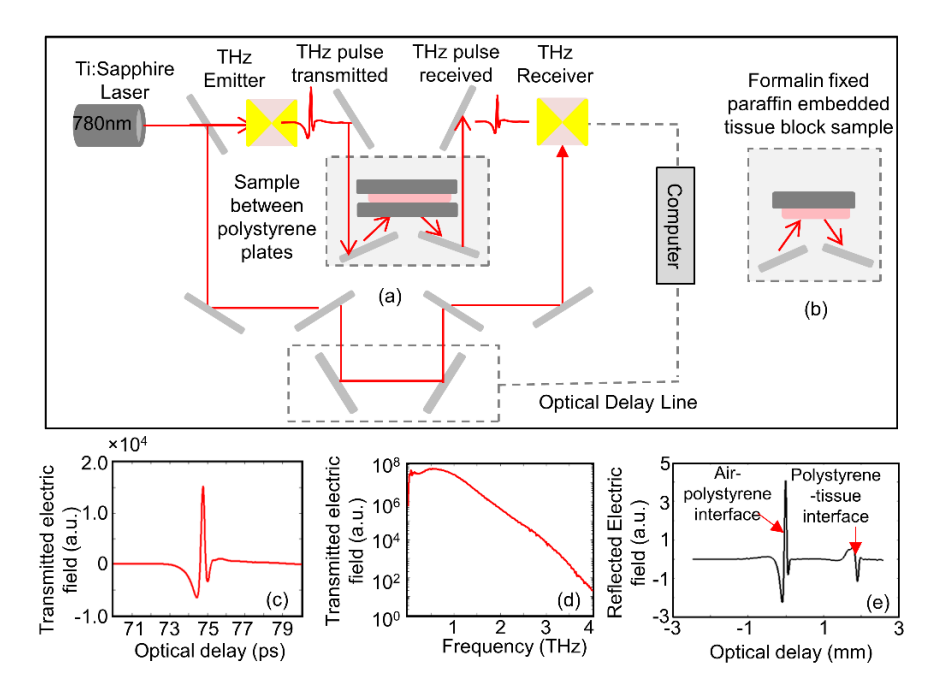


Fig. 1. Terahertz system diagram in reflection mode (a) for fresh tissue placed between two polystyrene plates, (b) for FFPE tissue block, (c) Time domain THz pulse, (d) Fourier transform of the THz pulse in (c), and (e) Reflection signals from the polystyrene-tissue arrangement in (a).

interface, Fig. 1e. To record the reflected data from the tissue, the first pulse is windowed-out, and only the second pulse is recorded at each pixel on the tissue [20]. In this case, the power spectra image is constructed across a frequency range from 0.5 THz to 1.0 THz as:

Spectral power =
$$\int_{0.5 \text{ THz}}^{1.0 \text{ THz}} \frac{|E_{\text{samp}}(f)|^2}{|E_{\text{ref}}(f)|^2} df$$
 (1)

where E_{samp} is the magnitude of the Fourier transform reflected sample signal, E_{ref} is a single point reference signal obtained from the air-polystyrene interface, and f is the frequency in THz. For the FFPE block tissue imaging, the block is placed directly onto the scanner, and the reflected time domain peak signal is collected at each pixel to construct the time domain THz image [17].

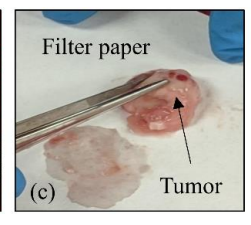
2.3 Pre-image Preparation of Fresh Tumor Tissue

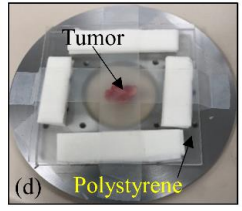
Upon excising the tumor from the rat with adequate healthy normal margin, it was immersed in phosphate buffered saline (PBS) for transfer from the excision site to the THz lab in the same building. As shown in Fig. 2a, the bulk tumor was bisected into two halves, such that each section has surrounding healthy normal tissue in Fig. 2b.

For performing the THz imaging, the tumor was first dried for around 3-4 minutes on a grade-1 filter paper, Fig. 2c. The tumor section was then positioned between two polystyrene plates with gentle pressure from the top to make the tumor surface as flat as possible for imaging, as shown in









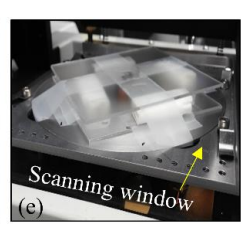


Fig. 2. Rat # 1 fresh tissue preparation for THz imaging. (a) Photograph of bulk tumor excised from rat tumor #1, (b) Bulk tumor bisected into two halves, (c) Tumor placed on filter paper to remove excess fluid, (d) Tumor positioned between two polystyrene plates, and (e) Polystyrene-tumor-polystyrene arrangement placed on the scanning window.

Fig. 2d. This tissue arrangement was then placed on the scanning window prepared for the reflection imaging, Fig. 2e. The x-y scanner motors were set to increment at every 200 μm step size to collect reflection data at each pixel on the specimen [20]. After completing the scanning, the tissue was immersed in a 10% buffered formalin solution and shipped to the Oklahoma Disease Diagnostic Laboratory for the histopathology process. In the histopathology process, all the fluid and lipids were extracted from the tissue (dehydrated tissue). Finally, the tumor was embedded in a paraffin block from which a 3-4 μm thick flat tissue section was sliced, stained with standard hematoxylin and eosin (H&E) ink, and fixed on glass slides. The FFPE tissue block and the H&E stained tissue glass slides are imaged using the THz reflection imaging system and the Nikon SMZ745T and NIKON Eclipse Ci microscopes, respectively. The scanner motors in the THz system were first set up to 400 μm step size to obtain quick images for adjusting the boundaries, but a finer step size of 200 μm was used to obtain the final THz images shown in this work.

2.4 Image Segmentation Based on the Expectation Maximization Technique

The THz images were assessed with respect to the pathology images as the ground truth of tumors. However, a pathology image has an inherently higher resolution than the THz image. Additionally, due to the dehydration process that the sample goes through during the histopathology process, a shape mismatch occurs between the pathology image and the THz image of fresh tissue [30]. Due to these factors and to compare the two images at a neutral ground, two statistical processes are implemented. First, a mesh morphing algorithm is used to digitize the pathology image and generate a classification at the same resolution and orientation as the THz image as reported in [12]. Our algorithm in [12] is implemented here to correct the alignment, resolution, and shape mismatch between these images. Such an algorithm utilizes control points within the contour of the images to provide a reference pathology for the pixel-by-pixel evaluation of the segmentation

results. The obtained image is referred to as the morphed pathology image. Second, a segmentation algorithm, based on the expectation maximization (EM) technique, is implemented on the THz image data to classify different tissue regions in the sample [31, 32]. The segmentation algorithm utilizes the amplitude of the frequency domain representation of the reflected THz waveform for each pixel, $v_n \in \mathbb{R}^F$, where F is the number of frequency samples in the spectrum, $n = \{1, ..., N\}$ is the index of the pixel of interest, and N corresponds to the total number of pixels in the THz image. The THz information for each pixel is represented by a high-dimension vector with F =106 frequency samples, which contains valuable information for the region characterization of the tumor. On the other hand, the high dimension of the THz information vector can negatively impact the model complexity of the segmentation process. Unlike alternative studies that summarize the THz information per pixel into a single physical characteristic, such as the absorption coefficient [33], the proposed algorithm employs a dimension reduction approach to identify the most relevant discriminating features while minimizing the loss of information. Here we utilize the lowdimensional ordered orthogonal projection (LOOP) algorithm [28], which empirically projects the high-dimension waveform per pixel into a lower-dimension subspace containing the most relevant features for the region segmentation of the THz image. The details of the LOOP algorithm and the EM technique were reported in [28, 34]. In addition to implementing the EM technique, we applied other classification methods such as estimating the model parameters within the Gaussian mixture model (GMM) utilizing a Markov chain Monte Carlo (MCMC) process. This procedure iteratively takes samples from the posterior distributions of the mixture model parameters by employing a Gibbs sampling technique [35]. Two versions of the MCMC were tested on the data (not presented due to space limitation); a 1-

157

158

159

160

161

162

163

164

165

166

167

168

169

170

171

172

173

174

175

176

177

178

179

dimensional MCMC [11] and a higher dimensional MCMC with LOOP [28]. The first algorithm

summarizes the THz waveform per pixel into a single feature, which corresponds to the spectral power and the peak of the normalized reflected signal for fresh and FFPE tissue, respectively [11]. While the second algorithm employs the LOOP dimension reduction technique to summarize the THz waveform per pixel into a lower dimension representation of the data with at least two features. A previous study compared the segmentation results obtained through EM and MCMC for the detection of breast cancer in THz imaging and concluded that the EM algorithm presents the best overall segmentation performance among these approaches [28]. It is important to clarify that the samples presented in this paper were analyzed by considering different dimension sizes within the LOOP algorithm, ranging from two to six dimensions. For consistency, we present the EM results obtained through the dimension size that achieved the best overall detection performance.

3 Experimental and Image Analysis Results

A total of 9 tumors were obtained from 20 ENU induced Sprague Dawley rats, while the rest did not produce any tumors in the expected period of 9-21 weeks and were sacrificed according to the protocol. The obtained tumors were bisected into two sections, as shown in Fig. 2. The low power pathology images of 17 tumor sections obtained from the 9 rat tumors are presented in Fig. 3. The details of the low power pathology process of stitching are clarified in Appendix A. The microscopic images of Figs. 3a-3q shows that the rat tumors exhibit cancer tissues adjacent to pre-existing normal fibro-fatty tissue with healthy mammary ducts and glands, mimicking the human breast tissue reported in [3, 17-20]. The microscopic images of Figs. 3a, b, f, g, j, l, m, and o, exhibit muscle tissue adjacent to both cancer and healthy fibro-fatty tissues. The muscle tissue is usually not present in human breast cancer excision but could exist in animal model tumors due to the narrow space where the tumor grows in the mammary pad.

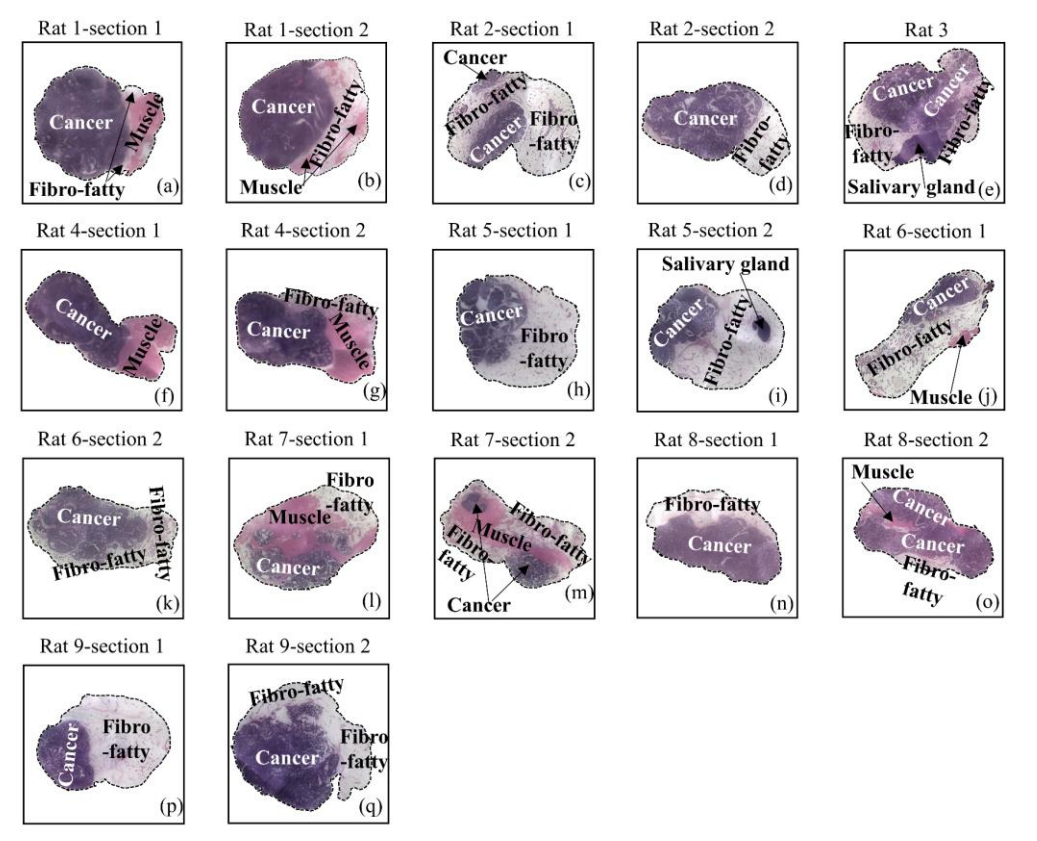


Fig. 3. Low power microscopic images of 17 tumor sections obtained from 9 rat tumors. (a) rat #1- section 1, (b) rat #1- section 2, (c) rat #2- section 1, (d) rat #2- section 2, (e) rat #3, (f) rat #4- section 1, (g) rat #4- section 2, (h) rat #5- section 1, (i) rat #5- section 2, (j) rat #6- section 1, (k) rat #6- section 2, (l) rat #7- section 1, (o) rat #8- section 1, (o) rat #8- section 2, (p) rat #9- section 1, and (q) rat #9- section 2.

Due to the space limitation, we present results for THz images and EM classifications for only three cases of ENU- rat tumors— rat tumor #1- section 2, rat tumor #2- section 2, and rat tumor #9- section 2.

3.1 THz Reflection Images

The THz reflection imaging of fresh and FFPE block tumor tissue are presented in Fig. 4. In addition, data of two tumors obtained from our previous mice models [13, 14] are included in the figure for comparison purposes. The first row of Fig. 4 shows the photographs of the fresh tissues starting with rat tumor #1- section 2 in Fig. 4a, rat tumor #2- section 2 in Fig. 4e, rat tumor #9-

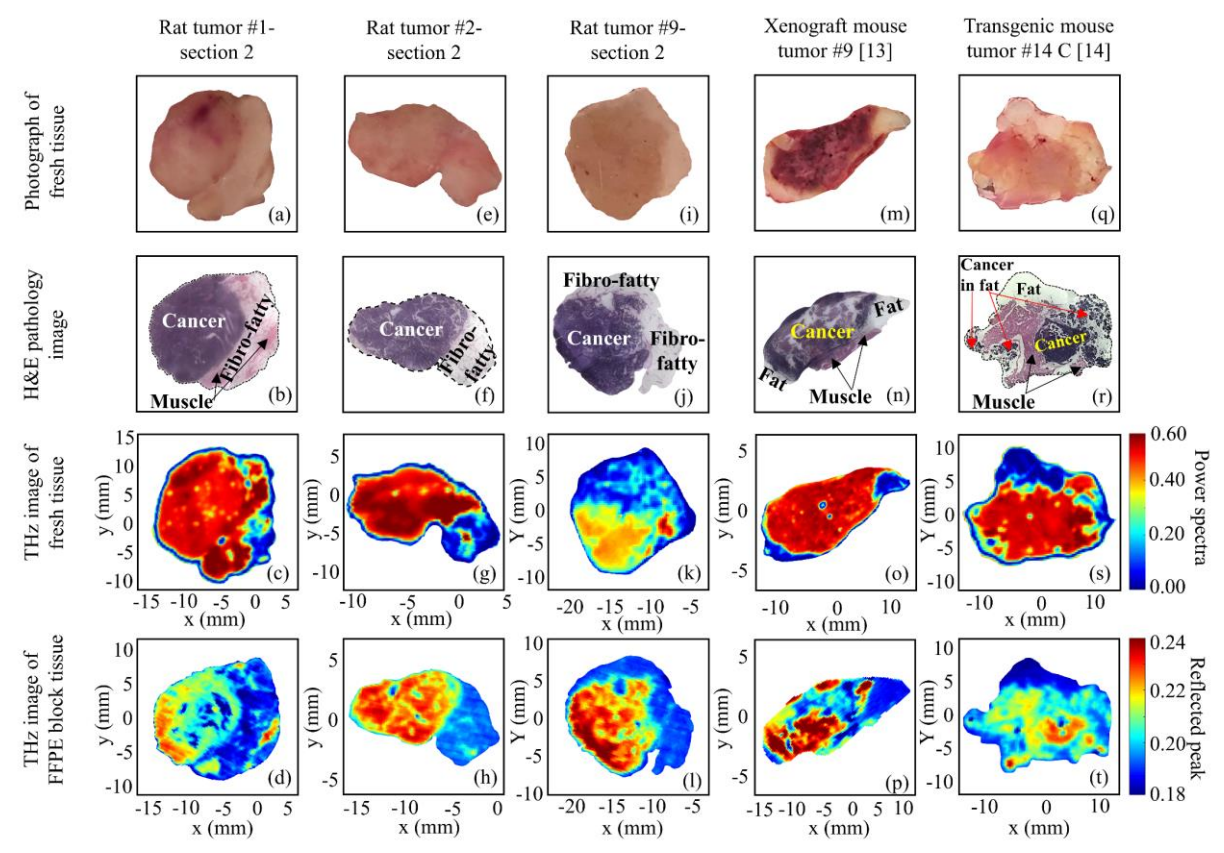


Fig. 4. THz reflection imaging results. For rat tumor #1- section 2 (a) the photograph of the fresh tissue, (b) the low power pathology image, (c) the THz power spectra image of the fresh tissue, (d) the THz time domain peak reflection image of the FFPE block. For rat tumor #2- section 2 (e) the photograph of the fresh tissue, (f) the low power pathology image, (g) the THz power spectra image of the fresh tissue, (h) the THz time domain peak reflection image of the FFPE block. For rat tumor #9- section 2 (i) the photograph of the fresh tissue, (j) the low power pathology image, (k) the THz power spectra image of the fresh tissue, (l) the THz time domain peak reflection image of the FFPE block. For xenograft mouse tumor #9- section 2 (m) the photograph of the fresh tissue [13], (n) the low power pathology image [13], (o) the THz power spectra image of the fresh tissue [13], (p) the THz time domain peak reflection image of the FFPE block [13]. For transgenic mouse tumor #14 C (q) the photograph of the fresh tissue [14], (r) the low power pathology image [14], (s) the THz power spectra image of the fresh tissue [14], and (t) the THz time domain peak reflection image of the FFPE block [14]. Figs. 4m-4p, are reproduced with permission from the IEEE. Figs. 4q-4t, are reproduced with permission from the IOP Publishing, Ltd.

section 2 in Fig. 4i, xenograft mouse tumor #9- section 2 [13] in Fig. 4m, and transgenic mouse tumor #14 C [14] in Fig. 4q. Following the same order, the results in the second, third, and fourth rows of Fig. 4 show the low power microscopic pathology images of H&E stained slide (second row), THz power spectra images of the freshly excised tumors (third row), and THz peak time reflection images of the FFPE block tumors (fourth row).

Upon visual inspection of the microscopic images of xenograft and transgenic mice sections in Figs. 4m and 4q, respectively, the differentiation between cancerous and non-cancerous tissues can be clearly observed. Whereas it is not the case for the ENU-rat tumor photographs in Fig. 4a, 4e, and 4i. Here we can see the advantageous role of utilizing the THz reflection imaging technology to highlight the contrast differentiation between cancerous and non-cancerous tissue sections in the tumors, as shown in Fig. 4.

216

217

218

219

220

221

222

223

224

225

226

227

228

229

230

231

232

233

234

235

236

237

238

The tumor of rat #1 was excised on the 63^{rd} day after the chemical injection with a size of ~ 18 mm diameter. The microscopic low power image in Fig. 4b shows that this tumor exhibits three tissue regions— cancer, fibro-fatty, and muscle. The light purple colored spots seen in the pathology image in Fig. 4b indicate a lack of cancer tissue on the slide (gaps) that is important to mention as it will also be seen in the THz image in Fig. 4d. These gaps could be either pre-existing lumens, which were filled with some secretions when the tissue was fresh, or occurred due to handling the tissue during the histopathology process. Fig. 4c shows the THz imaging of the fresh tumor obtained using the power spectra image using eq. (1) demonstrating the excellent distinction between cancer and the fibro-fatty regions of the tumor. Here, the cancer shows higher reflections (red color) than the fibro-fatty (cyan and blue color). However, no distinction could be observed between the cancer and the muscle regions. This is because the electrical properties of fresh muscle tissue and fresh cancer tissues are similar, in agreement with our previously reported work [11]. In contrast to the fresh tissue THz image, the THz peak reflection image in Fig. 4d shows a clear differentiation between all three regions, with cancer representing higher reflections (red color) followed by the muscle (light yellow) and fat (blue color). Consistent with the pathology image in Fig. 4b, the THz image in Fig. 4d shows blue color spots inside the cancer region associated with the gaps/lumens filled with the paraffin.

The rat tumor #2 was excised on the 68th day from the chemical injection with a ~11.87 mm tumor diameter. Based on the microscopic image in Fig. 4f, this tumor includes two tissue regions— cancer and fibro-fatty. Here, we also observe in Fig. 4g that the THz power spectra image shows higher power spectra values for the cancer region (red color) compared with the fibro-fatty region (blue and cyan color). In other words, a clear margin between cancer and fibro-fatty tissue regions is seen in this image. This differentiation is also observed in the THz peak reflection image of the FFPE block tumor in Fig. 4h, with cancer demonstrating higher reflection magnitude (red color) than the fibro-fatty region (blue and cyan color). Furthermore, we observe darker red color regions (higher reflection) in the cancer region in Figs. 4c and 4g that could be due to higher density of cancer cells, insufficient drying of the tumor before placing it on the polystyrene plate, or excess fluid secreted out of the tumor due to the pressure from the polystyrene plate during the scanning process.

The third case presented here is for the rat tumor #9 shown in Figs. 4i-4l. This tumor was excised on the 120th day after the chemical injection with a tumor diameter equals to ~10.63 mm. Like the second rat tumor, this tumor also exhibits cancer and fibro-fatty regions, as shown in the microscopic image of Fig. 4j. Consistent with the above cases, the THz power spectra image in Fig. 4k and the peak reflection image in Fig. 4l demonstrate higher reflection values for the cancer region (yellow-red color) in the tumor compared with the fibro-fatty region (blue and cyan color). Upon comparing the THz image of the FFPE block tissue in Fig. 4l and the pathology image in Fig. 4j, we see an excellent qualitative correlation between both images. However, this is not the case with the fresh tissue image. As discussed in our previous work [30], the histopathology process introduced deformation in tissue shape leading to a change in the imaging surface. Therefore, the correlation between the fresh tissue THz image and pathology image is degraded.

For comparison purposes between three animal breast tumor models, two tumors of different animal models based on mice are included in Fig. 4. The first is the xenograft mice model reported in [11-13], and the transgenic mice model reported in [14]. These three breast cancer animal models represent major differences in the tumor growth process, types of healthy tissues enclosed in the tumor along with cancer, the heterogeneity of the tumor, and the amount of healthy tissue at the tumor margin. As described in Section 2.1, the tumors in the Sprague Dawley rats were induced by injecting ENU chemical in the rat's mammary pad. Whereas the tumors in C57BL/6 black laboratory xenograft mice were induced by injecting E0771 murine breast adenocarcinoma cells in their mammary pad [13]. In contrast to both these methods, the transgenic model did not require any carcinogen injection to induce tumors in the mice's body as it is a genetically modified mice model that grows multifocal tumors spontaneously in the mammary pad [14].

The data of the xenograft and transgenic tumors are shown in Figs. 4m-4t. As observed from the THz imaging point of view, we see a visual consistency in differentiation between different tumor regions. For example, in the THz power spectra image of xenograft mouse tumor #9 in Fig. 4o and the transgenic mouse tumor #14 in Fig. 4s, the cancer shows higher reflections (red color) compared with fat (blue color). Also, like rat tumor #1, the cancer and muscle show similar reflection magnitudes in the fresh tissue images in Figs. 4o and 4s. We also observed consistent THz reflections from different regions in the FFPE block tissue images in Figs. 4p and 4t, for xenograft mouse and transgenic mouse tumors, respectively.

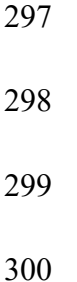
Furthermore, upon comparing the microscopic images of xenograft [13] and transgenic [14] mice tumors in Figs. 4n and 4r, respectively, with the microscopic images of rat tumors in Fig. 3, it can be seen that both mice tumor models lack the presence of pre-existing healthy fibrous tissue in the excised tumors. Both mice tumor models exhibit only fat adjacent to cancer in the tumor.

Also, it can be seen that the amount of surrounding healthy tissue available in ENU-rat tumors is more than that in the presented mice models.

A numerical comparison between the percentage cancerous pixels in each tumor in three animal models is shown in Table 1 and Fig. 5. The percentage is achieved through generating binary masks of the tissue under test. The outer mask of the FFPE block is obtained upon mapping the THz image with the pathology image, while the fresh tissue mask was obtained through applying the gradient to the fresh tissue THz image. The binary masks have values of one for the pixels on the tissue and zeros for the outside pixels. Similarly, a second binary mask is generated for the cancerous region using the guidance of the pathology image for the FFPE tumor and the gradient for the THz fresh tissue. The estimated percentage of cancerous pixels is comparable among the tumors indicating to a general preservation of the surface between the fresh and fixed tissue specimens. Furthermore, despite the very different procedures used to grow the tumors in

Table 1: Summary of % cancerous pixels in each tumor in Fig. 4

Tumor Type	% of cancer pixels in fresh tumor	% of cancer pixels in FFPE block tumor	
Rat #1- section 2	56.61	50.7	
Rat #2- section 2	73.22	65.99	
Rat #9- section 2	46.12	54.33	
Xenograft #9- section 2 [13]	62.70	68.71	
Transgenic #14 C [14]	43.09	45.81	



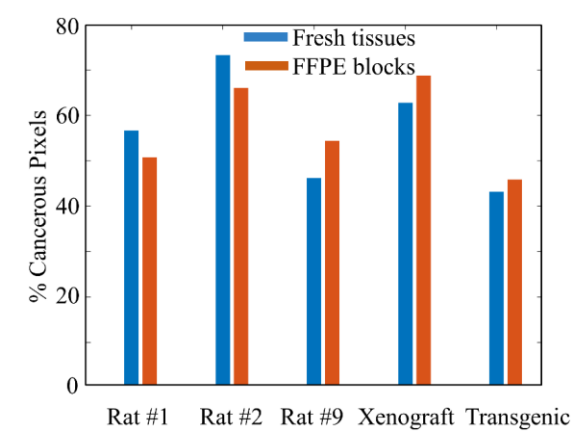


Fig. 5. Percentage of cancerous pixels in each tumor THz image in Fig. 4.

these three animal models, the percentage of cancerous pixels is consistent with the size of the excised tumors following the IACUC protocol.

3.2 THz Image Classification

The tumor classification results in Fig. 6 are achieved using the EM technique for all tumors presented in Fig. 4. While the THz images of xenograft and transgenic mice tumors are published in [13, 14], the EM classification technique is implemented on these mice tumors here for the first time for comparison purposes. The results are obtained from a binary classification perspective as cancer versus non-cancerous regions, in which any non-cancerous regions in the tumor are merged into a single region. For the binary representation of tumors in Fig. 6, cancer pixels in each tumor are displayed as red color and the non-cancer pixels (fat, fibro, or muscle tissues) as blue color.

The statistical classification results of rat #1 are presented in Figs. 6a-6d. The morphed pathology images, constructed based on the pathology assessment, are obtained separately for both fresh and FFPE tumors [12], as shown in Figs. 6a and 6c, respectively. The EM model results are shown in Figs. 6b and 6d for the fresh and FFPE tissue, respectively. Although there is no tissue distortion among the pathology results and the THz image of the FFPE tissue, the morphing algorithm is still applied to the FFPE tissue to correct the resolution and alignment mismatch between these images. For this tumor, the fibro-fatty and muscle tissues are grouped together and classified as non-cancer for the binary representation of the tissue classification results. The results in Fig. 6b represent the classification of tissues in the fresh tumor obtained by the 3D EM model. It can be observed here that the 3D EM segmentation model presents a good visual correlation with respect to the morphed pathology results, where it identifies the cancerous area correctly with minimum non-cancer misclassification. The classification image shown in Fig. 6d represents the

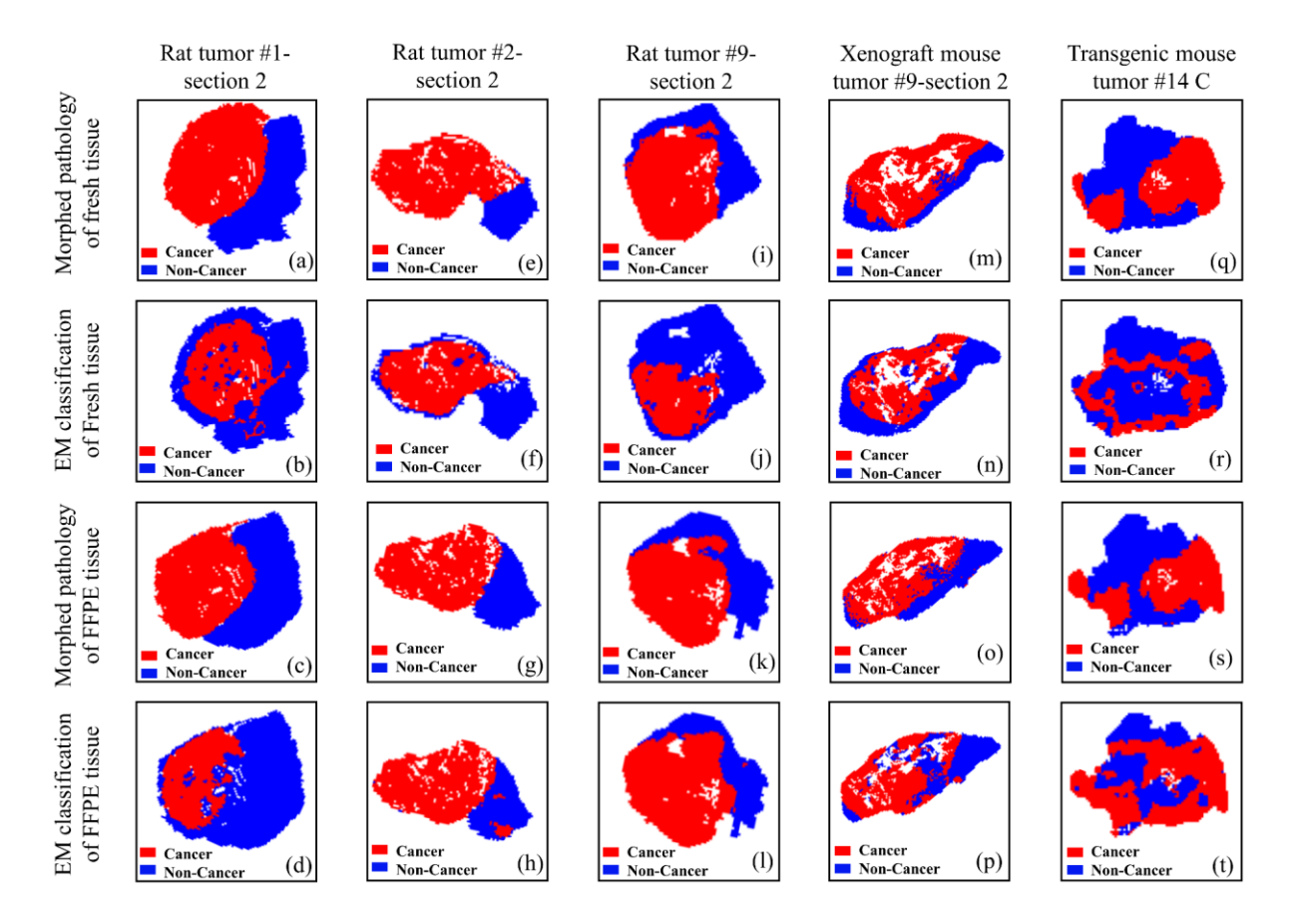


Fig. 6. Statistical classification. Sub-figures (a-d) for rat #1; (a) The morphed pathology for the fresh tissue, (b) The 3D EM detection model results for the fresh tissue, (c) The morphed pathology image for the FFPE tissue block, and (d) The 4D EM detection model results for the FFPE block tissue. Sub-figures (e-h) for Rat # 2; (e) The morphed pathology for the fresh tissue, (f) The 2D EM detection model results for the fresh tissue, (g) The morphed pathology image for the FFPE tissue block, and (h) The 4D EM detection model results for the FFPE block tissue. Sub-figures (i-l) for rat #9. (i) The morphed pathology for the fresh tissue, (j) The 2D EM detection model results for the fresh tissue, (k) The morphed pathology image for the FFPE tissue block, and (l) The 4D EM detection model results for the FFPE block tissue. Sub-figures (m-p) for xenograft mouse #9. (m) The morphed pathology for the fresh tissue, (n) The 2D EM detection model results for the FFPE block tissue. Sub-figures (q-t) for transgenic mouse #14 C. (q) The morphed pathology for the fresh tissue, (r) The 2D EM detection model results for the fresh tissue, (s) The morphed pathology image for the FFPE tissue block, and (t) The 2D EM detection model results for the fresh tissue, (s) The morphed pathology image for the FFPE tissue block, and (t) The 2D EM detection model results for the FFPE block tissue.

FFPE block tumor segmentation results obtained using the 4D EM model. In this figure, we can observe that the 4D EM segmentation results show some misclassification of the non-cancer region but overall shows a good correlation with the microscopic image in Fig. 4a.

The statistical classification results of rat tumor #2 are discussed in Fig. 6e-6h. The morphed pathology image of a fresh and FFPE tumor in Fig. 6e and 6g display cancer and fibro-fatty tissue

regions in the tumor as cancer and non-cancer, respectively. The 2D EM classification model results for fresh tumor THz data are presented in Fig. 6f. By visually inspecting Fig. 6f, we can observe that the overall region classification for the EM model shows a good correlation with the morphed pathology results with a very minimum non-cancer misclassification around the edge of the cancer region. Furthermore, the classification results obtained for the FFPE block tumor using the 4D EM model are presented in Fig. 6h. This figure shows that the model represents the correct classification of both cancer and non-cancer regions with a small region of pixels in the non-cancer region classified as cancer. These results are to be compared with the pathology and THz images of rat # 2 in Fig. 4.

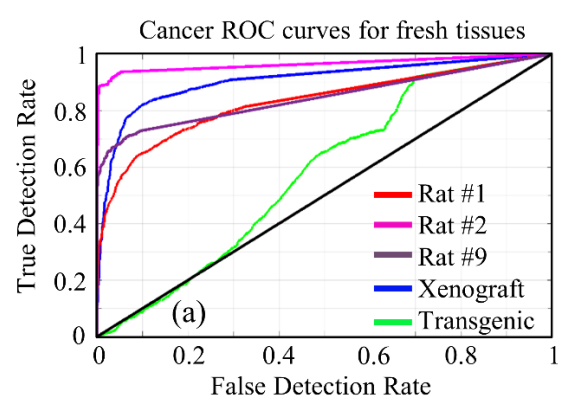
The statistical classification results of the third tumor, rat tumor #9, are shown in Fig. 6i-6l. The morphed pathology images of fresh and FFPE tumors showing a binary representation of tumor as cancer and non-cancer regions are shown in Figs. 6i and 6k, respectively. By visually inspecting the 2D EM classification results in Fig. 6j, we can observe that most of the cancer area located in the lower-left section of the tissue was correctly identified. In contrast, the upper-middle cancerous region within the tissue was mostly misclassified. For the FFPE block tumor, the segmentation image obtained using the 4D EM model presented in Fig. 6l represents the correct classification of both cancer and non-cancer regions. These results are to be compared with the microscopic pathology and THz images of rat # 9 in Fig. 4.

The statistical classification results of the xenograft mouse tumor #9 are shown in Fig. 6m-6p. In the morphed pathology images of fresh and FFPE block tumor in Fig. 6m and 6o, respectively, the fat and muscle tissues are combined and displayed as non-cancer. From the classification imaging results in Fig. 6n, we can observe that the overall region classification for the 2D EM model presents a good correlation with the morphed pathology results and correct classification of

muscle as a non-cancer region around the lower-middle edge of the cancer region. The 3D EM model deployed for the FFPE block tumor provides the correct classification of both cancer and non-cancer regions with some misclassification of cancer in the upper right section of the tumor, as presented in Fig. 6p.

Similarly, the classification results of the fifth tumor obtained from transgenic mouse #14 are presented in Figs. 6q-6t. In the morphed pathology images in Figs. 6q and 6s for fresh and FFPE block tumors, respectively, the cancer and cancer in fat are grouped to be classified as cancer, and fat and muscle tissues are grouped to be classified as non-cancer. The segmentation results for the fresh transgenic tumor obtained using the 2D EM model in Fig. 6r represent the misclassification of the cancer area located in the center of the tumor. Similarly, in the 2D EM classification results of FFPE tumor shown in Fig. 6t, the non-cancer region in the upper-left and lower-left region of the tumor is misclassified as cancer.

The segmentation process shown above is performed by considering the total number of regions within the tissue, but the performance analysis presented here is evaluated in terms of the detection of cancer alone using the operating characteristic (ROC) curves. Ideally, the ROC curves achieve the optimum 100% true detection rate with 0% false detection rate. Therefore, we compare the proposed classifiers' performance by analyzing their proximity to the optimal detection point within the curve. Additionally, we summarize the classifiers' performance by obtaining their areas under the ROC curve, which are then evaluated by considering their proximity to the ideal case, i.e., 100%. A comparison of the ROC curves of cancer for the rats, xenograft mouse, and transgenic mouse is summarized in Fig. 7 and Table 2. In Fig. 7, we present the cancer ROC curves obtained using the statistical EM classification technique of the five tumors presented in Fig. 4. The cancer



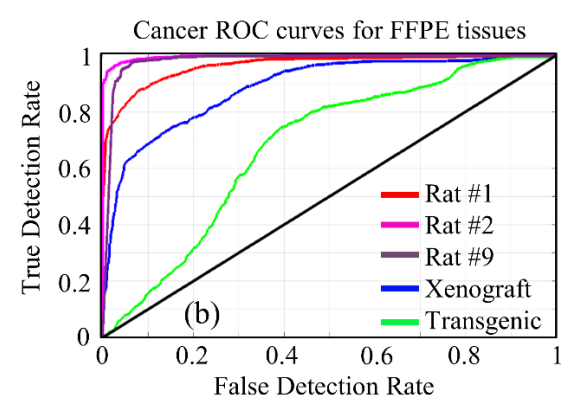


Fig. 7. ROC curves of cancer using the EM technique. (a) fresh tissues, and (b) FFPE tissues.

ROC curves for fresh tissue samples are presented in Fig. 7a and for the FFPE block tissue samples in Fig. 7b.

As mentioned in the Methodology Section, the tumor sections were also classified using the MCMC method, and the areas under the cancer ROC curves are listed in Table 2. Upon comparing the MCMC and EM results, it is clear that the EM technique provided the highest success rate in most of the cases. For example, the EM provided 96.45 % for rat tumor # 2, followed by the xenograft mouse tumor # 9 with 90.68 %. The classifications of rat tumors # 1 and # 9 show similar performance with more ~84 % area under the ROC curve. The performance of the classifier in the

Table 2: Summary of areas under the cancer ROC curves for all samples

Fresh Tissue		FFPE Block Tissue				
Rat Tumor #1 Section 2						
1D MCMC	6D MCMC	3D EM	1D MCMC	2D MCMC	4D EM	
0.7787	0.8392	0.831	0.7551	0.9347	0.9636	
Rat Tumor #2 Section 2						
1D MCMC	2D MCMC	2D EM	1D MCMC	6D MCMC	4D EM	
0.9591	0.9284	0.9645	0.9752	0.9949	0.9957	
Rat Tumor #9 Section 2						
1D MCMC	5D MCMC	2D EM	1D MCMC	5D MCMC	4D EM	
0.7319	0.8356	0.8457	0.9312	0.9711	0.9812	
Xenograft Tumor #9 Section 2						
1D MCMC	2D MCMC	2D EM	1D MCMC	2D MCMC	3D EM	
0.8647	0.8968	0.9068	0.8633	0.8827	0.8869	
Transgenic Tumor #14 C						
1D MCMC	5D MCMC	2D EM	1D MCMC	3D MCMC	2D EM	
0.624	0.6551	0.5782	0.5917	0.6878	0.6776	

rat tumor # 9 could be degraded due to the distortion in the shape of the tumor after the histopathology process, as discussed earlier. Furthermore, we observe that the transgenic mouse tumor #14 C does not show good tissue classification due to the high heterogeneity and complexity observed in the transgenic tumors, as reported in [14]. As cancer invades the other tissue, it became difficult for the classifier to distinguish between the different regions of the transgenic model. Similarly, the EM classification of FFPE block tumors in Fig. 7b presents the best performance among the rat tumors. The results of Table 2 show a success rate with more than 95% area under the ROC curves for rat tumors, followed by xenograft mouse tumor #9 with 88.69%, and then the transgenic mouse tumor with 67.76%. The results of Table 2 are consistent with the classification results of human breast cancer tumors reported in [28].

4. Conclusion and Future Work

The results obtained in this work highlighted the THz imaging reflection technique and the expectation maximization classification (EM) algorithm of breast cancer in rats. Malignant mammary tumors were grown in Sprague Dawley rats upon injection with the N-ethyl-N-nitrosourea (ENU).

Seventeen tumor sections were obtained from nine tumors once they reached the size of ~18mm in diameter. The freshly excised tissue sections and their associated dehydrated FFPE block tissues were scanned on the imaging system to produce the THz images. The fresh tissue images were based on the reflected signal in the frequency domain using the power spectra formulation, while the FFPE block tissue images were based on the peak of the time domain reflected signal at each pixel. The low power microscopic images of the 17 rat tumor sections were obtained using the high-power microscope, followed by applying the stitching procedure. The obtained images demonstrate that the ENU-tumors induced in rats exhibit the presence of cancer tissue adjacent to

healthy fibro-fatty tissues like human breast cancer tumors. This was the motivation of this work as the previously investigated xenograft, and transgenic mice tumor models did not exhibit such resemblance with human breast tumors.

Based on the results obtained in this work, we can conclude that the xenograft tumor model represents the simplest tumor with only cancer and fat regions. The transgenic model represents much more complex heterogeneous tumors with cancer invading the surrounding tissue and expressing advanced-stage tumors. At the same time, the ENU-tumor rat model fits in between the two mice models and closely mimics human breast tumors where healthy fibro-fatty tissues are present adjacent to cancer tissues.

The obtained THz images showed significant differentiation between cancer and healthy tissues in most tumors' sections presented here. A few sections showed the presence of muscle tissue in the tumor, which exhibits reflection signals like the cancer in the THz images shown in Fig. 4. As a result, the presence of muscle tissue introduced some challenges in the EM classification; however, muscle tissue is not a concern in human breast tumors. While THz images of the FFPE block tissue show a good correlation with the pathology image, the challenge remains in the correlation between the THz image of fresh tissue and the pathology image. As reported in previous work [30], there is usually a surface mismatch between the pathology and the fresh tissue THz image, as can be clearly seen in rat tumor #9- section 2. The primary reason for this mismatch is due to tissue deformation that occurs during the histopathology process. Almost ~100 µm thick tissue section is usually removed during the histopathology process to obtain a flat surface cut for the H&E stained slide. The mismatch and deformation in the imaging surface lead to a mismatch in the image between THz and pathology. Additionally, during the histopathology process, the tissue sometimes gets unfold and laid down at the bottom surface of the tumor. This also introduces

ambiguity when correlating fresh tissue THz images with the pathology image. This observation is consistent with our previous mice tumor models [13, 14].

THz imaging and classification results were obtained for the ENU-tumors in rats and the mice models previously published, such as the xenograft [11-13] and the MMTV PyMT transgenic [14]. The difference observed in the results between these animal models was based on various factors, like the tumor induction process, the presence of healthy breast tissue at the tumor's margin, the tissue types in the tumor, and the tissue response to the THz pulse. A small amount of fibrous tissue was exhibited in transgenic mouse tumors, but that fibrous tissue was cancer induced tissue and not pre-existing. The results also showed that the best classification was achieved using the EM technique, except for the transgenic mouse tumor, consistent with the classification of human breast cancer tumors reported in [28]. Furthermore, the obtained results showed that the EM classification of cancer in freshly excised tumors seems to be underpredicted by showing more false negatives than false positives.

The future work focuses on implementing machine learning and deep learning algorithms on THz imaging to perform better cancer classification and better assessment of tumor margins. Machine learning, as known, requires establishing a large database of tumor tissues. The use of ENU-tumor in rats has shown a potential to provide an adequate amount of data instead of relying on human breast tumors. Furthermore, a spectroscopy procedure in the reflection mode will be conducted to extract the refractive index and absorption coefficient of the xenograft, transgenic, and rat tumor models and compare with human breast tumors.

Append A: Microscopic Imaging and Image Analysis

The analysis of each rat mammary tumor is performed via microscopic imaging of the H&E-stained tissue slide (Fig. 8a). The first step in this process is to construct the low power microscopic

image of the tissue slide. This is achieved by taking ~ 10-15 subsection images of the H&E slide at 6.7x magnification, as shown in Fig. 8b. The size of each sub-image obtained at 6.7x magnification is 3.28 × 3.28 mm. The images are taken such that every two adjacent subsection images have a common region between them. These images are then uploaded in open-source software (Hugin-Panorama Stitcher [36]). To map the common regions among all images, one image is taken as a reference image and is compared one on one with other images. For example, in Fig. 8c, image #1 is taken as a reference image, and it is further compared with all other images. The common regions between the reference image and the other images are marked as different colored boxes in Fig. 8c. Every image is made a reference image, and this mapping process is repeated for all images. Upon completion of the common region mapping process, the software then compiles the stitching of the images to provide the complete pathology image of the tissue at

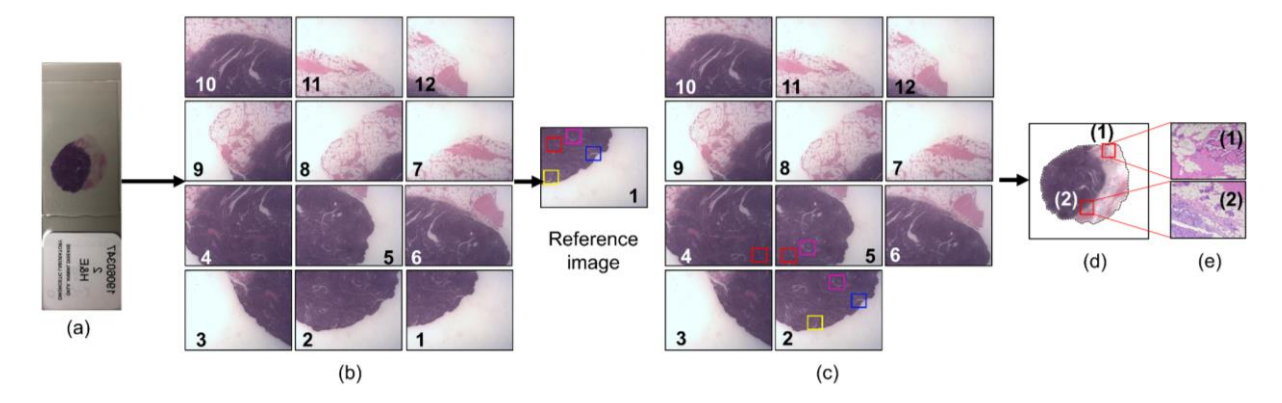


Fig. 8. Stitching microscopic images of mammary tumor from rat # 1. (a) H&E-stained tissue slide of rat tumor #1- section 2, (b) Low power microscopic images of the slide in (a) at 6.7x magnification, (c) compiled image in the software after mapping of common points between all images in (b), (d) Stitched pathology image, and (e) High power images obtained at 100x magnification for the tissue regions marked (1) and (2) in (d).

6.7x magnification, as shown in Fig. 8d. To assess the tissue, few regions on the low power image are selected, for which 100x magnification images are obtained to have the cellular level information of the selected region. For example, at the regions marked (1) and (2) in Fig. 8d, the high-power images are presented in Fig. 8e. The size of each high-power image obtained at 100x

- 465 magnification is 0.22×0.22 mm. Several such images are taken that covers most of the tissue
- regions to be assessed.
- 467 Disclosures
- The authors declare that they have no conflict of interest.
- 469 Acknowledgments
- This work was funded by the National Institutes of Health Award No. R15CA208798. It was also
- 471 funded in part by the National Science Foundation (NSF) Award No. 1408007. Funding for the
- pulsed THz system was obtained through NSF/MRI Award No. 1228958. We also acknowledge
- 473 the collaboration with Oklahoma Animal Disease Diagnostic Laboratory at the Oklahoma State
- 474 University for conducting the histopathology procedure on all the tissues handled in this work. The
- 475 Authors also acknowledge the use of the Histopathology Lab in the Biomedical Engineering
- 476 Department at the University of Arkansas.
- 477 References
- 1. K. Okada, K. Serita, Q. Cassar, H. Murakami, G. MacGrogan, J-P. Guillet, P. Mounaix, and M.
- Tonouchi, "Terahertz near-field microscopy of ductal carcinoma in situ (DCIS) of the breast," Journal
- 480 of Physics: Photonics, vol. 2, no. 4, pp. 044008, 2020.
- 481 2. O. Sun, Y. He, K. Liu, S. Fan, E. P. J. Parrott, and E. Pickwell-MacPherson, "Recent advances in
- 482 terahertz technology for biomedical applications," *Quantitative Imaging in Medicine and Surgery*, vol.
- 483 7, no. 3, pp. 345-355, 2017.
- 484 3. T. Bowman, N. Vohra, K. Bailey, and M. El-Shenawee, "Terahertz tomographic imaging of freshly
- excised human breast tissues," *Journal of Medical Imaging*, vol. 6, no. 2, pp. 023501, 2019.

- 486 4. B. S. Peter, S. Yngvesson, P. Siqueira, P. Kelly, A. Khan, S. Glick, and A. Karellas, "Development and
- testing of a single frequency terahertz imaging system for breast cancer detection," *IEEE Journal of*
- 488 Biomedical and Health Informatics, vol. 17, no. 4, pp. 785-97, 2013.
- 489 5. S. Yamaguchi, Y. Fukushi, O. Kubota, T. Itsuji, T. Ouchi, and S. Yamamoto, "Brain tumor imaging of
- rat fresh tissue using terahertz spectroscopy," *Scientific Reports*, vol. 6, no. 1, pp. 30124, 2016.
- 491 6. H. Zuhayri, A. I. Knyazkova, V. V. Nikolaev, A. V. Borisov, Yu. V. Kistenev, O. A. Zakharova, P. A.
- Dyachenko, and V. V. Tuchin, "Study of wound healing by terahertz spectroscopy," *Proc. SPIE 11582*,
- 493 Fourth International Conference on Terahertz and Microwave Radiation: Generation, Detection, and
- 494 Application, Tomsk, Russian Federation, 115821E, 2020.
- 495 7. S. Sy, S. Huang, Y-X. Wang, J. Yu, A. T. Ahuja, Y-T. Zhang, and E. Pickwell-MacPherson, "Terahertz
- spectroscopy of liver cirrhosis: investigating the origin of contrast," *Physics in Medicine and Biology*,
- 497 vol. 55, no. 24, pp. 7587-96, 2010.
- 498 8. Y. C. Sim, J. Y. Park, K-M. Ahn, C. Park, and J-H. Son, "Terahertz imaging of excised oral cancer at
- frozen temperature," *Biomedical optics express*, vol. 4, no. 8, pp. 1413-21, 2013.
- 500 9. F. Wahaia, G. Valusis, L. M. Bernardo, A. Almeida, J. A. Moreira, P. C. Lopes, J. Macutkevic, I.
- Kasalynas, D. Seliuta, R. Adomavicius, R. Henrique, and M. Lopes, "Detection of colon cancer by
- terahertz techniques," *Journal of Molecular Structure*, vol. 1006, no. 1, pp. 77-82, 2011.
- 503 10. H. Chen, T-H. Chen, T-F. Tseng, J-T. Lu, C-C. Kuo, S-C. Fu, W-J. Lee, Y-F. Tsai, Y-Y. Huang, E. Y.
- Chuang, Y-J. Hwang, and C-K. Sun, "High-sensitivity in vivo THz transmission imaging of early
- human breast cancer in a subcutaneous xenograft mouse model," Opt. Express, vol. 19, no. 22,
- 506 pp.21552-62, 2011.
- 11. T. Bowman, T. Chavez, K. Khan, J. Wu, A. Chakraborty, N. Rajaram, K. Bailey, and M. El-Shenawee,
- "Pulsed terahertz imaging of breast cancer in freshly excised murine tumors," J. Biomed. Opt., vol. 23,
- 509 no. 2, pp. 026004, 2018.

- 510 12. T. Chavez, T. Bowman, J. Wu, K. Bailey, and M. El-Shenawee, "Assessment of terahertz imaging for
- excised breast cancer tumors with image morphing," J. Infrared Milli. Terahz Waves, vol. 39, no.
- 512 12, 1283–1302, 2018.
- 513 13. T. Chavez, T. Bowman, J. Wu, K. Bailey, and M. El-Shenawee, "Cancer classification of freshly
- excised murine tumors with ordered orthogonal projection," *Proc. 2019 IEEE International Symposium*
- on Antennas and Propagation and USNC-URSI Radio Science Meeting, Atlanta, GA, USA, pp. 525-
- 516 526, *2019*.
- 517 14. N. Vohra, T. Bowman, P. M. Diaz, N. Rajaram, K. Bailey, and M. El-Shenawee, "Pulsed terahertz
- reflection imaging of tumors in a spontaneous model of breast cancer," *Biomed. Phys. & Engg. Express*,
- 519 vol. 4, no. 6, pp. 065025, 2018.
- 520 15. C. T. Guy, R. D. Cardiff, and W. J. Muller, "Induction of mammary tumors by expression of
- 521 polyomavirus middle T oncogene: a transgenic mouse model for metastatic disease," *Molecular and*
- 522 *Cellular Biology*, vol. 12, no. 3, pp. 954-61, 1992.
- 523 16. E. Y. Lin, J. G. Jones, P. Li, L. Zhu, K. D. Whitney, W. J. Muller, and J. W. Pollard, "Progression to
- malignancy in the polyoma middle T oncoprotein mouse breast cancer model provides a reliable model
- for human diseases," *The American Journal of Pathology*, vol. 163, no. 5, pp. 2113-26, 2003.
- 526 17. T. C. Bowman, M. El-Shenawee, and L.K. Campbell. "Terahertz imaging of excised breast tumor tissue
- on paraffin sections," *IEEE Trans, on Ant. and Propag.*, vol. 63, no. 5, pp. 2088-2097, 2015.
- 528 18. T. Bowman, M. El-Shenawee, and L. K. Campbell, "Terahertz transmission vs reflection imaging and
- model-based characterization for excised breast carcinomas," *Biomed. Opt. Express*, vol. 7, no. 9, pp.
- 530 3756-83, 2016.
- 531 19. T. Bowman, Y. Wu, J. Gauch, L. K. Campbell, and M. El-Shenawee, "Terahertz imaging of three-
- dimensional dehydrated breast cancer tumors," J. Infrared Milli. Terahz Waves, vol. 38, no. 6, pp. 766-
- 533 786, 2017.
- 534 20. N. Vohra, T. Bowman, K. Bailey, and M. El-Shenawee, "Terahertz imaging and characterization
- protocol for freshly excised breast cancer tumors," J. Vis. Exp. issue. 158, pp. e61007, 2020.

- 536 21. K. Almholt, K. A. Green, A. Juncker-Jensen, B. S. Nielsen, L. R. Lund, and J. Rømer, "Extracellular
- proteolysis in transgenic mouse models of breast cancer," Journal of Mammary Gland Biology and
- *Neoplasia*, vol. 12, no. 1, pp. 83-97, 2007.
- 539 22. G. Stoica, A. Koestner, and C. Capen, "Neoplasms induced with high single doses of N-ethyl-N-
- nitrosourea in 30-day-old Sprague-Dawley rats, with special emphasis on mammary neoplasia,"
- 541 Anticancer research, vol. 4, no. 1-2, pp. 5-12, 1984.
- 542 23. P. Swann and P. Magee, "Nitrosamine-induced carcinogenesis. The alkylation of N-7 of guanine of
- nucleic acids of the rat by diethylnitrosamine, N-ethyl-N-nitrosourea and ethyl methanesulphonate,"
- *Biochemical Journal*, vol. 125, no. 3, pp. 841-7, 1971.
- 545 24. G. Stoica, A. Koestner, and C. Capen, "Characterization of N-ethyl-N-nitrosourea--induced mammary
- tumors in the rat," *The American journal of pathology*, vol. 110, no. 2, pp. 161, 1983.
- 547 25. K. Turetschek, T. P. Roberts, E. Floyd, A. Preda, V. Novikov, D. M. Shames, W. O. Carter, and R. C.
- 548 Brasch, "Tumor microvascular characterization using ultrasmall superparamagnetic iron oxide particles
- 549 (USPIO) in an experimental breast cancer model," J. Magn. Reson. Imaging, vol. 13 no. 6, pp. 882-8,
- 550 2001.
- 551 26. W. Li, R. B. Calder, J. C. Mar, and J. Vijg, "Single-cell transcriptogenomics reveals transcriptional
- exclusion of ENU-mutated alleles," Mutation Research/Fundamental and Molecular Mechanisms of
- 553 *Mutagenesis*, vol. 772, pp. 55-62, 2015.
- 554 27. A. Nazmeen and S. Maiti, "Oxidant stress induction and signalling in xenografted (human breast
- 555 cancer-tissues) plus estradiol treated or N-ethyl-N-nitrosourea treated female rats via altered estrogen
- sulfotransferase (rSULT1E1) expressions and SOD1/catalase regulations," *Molecular biology reports*,
- 557 vol. 45, no. 6, pp. 2571-84, 2018.
- 558 28. T. Chavez, N. Vohra, J. Wu, K. Bailey and M. El-Shenawee, "Breast cancer detection with low-
- dimensional ordered orthogonal projection in terahertz imaging," IEEE Transactions on Terahertz
- *Science and Technology*, vol. 10, no. 2, pp. 176-189, 2020.

- 561 29. A. P. Salinger, and M. J. Justice MJ, "Mouse mutagenesis using N-ethyl-N-nitrosourea (ENU)," CSH
- 562 *Protoc.* vol. 3, no. 4, Apr 2008.
- 30. M. El-Shenawee, N. Vohra, T. Bowman, K. Bailey, "Cancer detection in excised breast tumors using
- terahertz imaging and spectroscopy," *Biomedical Spectroscopy and Imaging*, vol. 8, no. 1-2, pp. 1-9,
- 565 2019.
- 31. S. Ragothaman, S. Narasimhan, M. Basavaraj, and R. Dewar, "Unsupervised segmentation of cervical
- cell images using gaussian mixture model," in *Proceedings of the IEEE Conference on Computer Vision*
- and Pattern Recognition (CVPR) Workshops, pp. 70-75, 2016.
- 32. J. Friedman, T. Hastie, and R. Tibshirani, *The Elements of Statistical Learning* (Springer Series in
- 570 Statistics), vol. 1. New York, NY, USA: Springer, 2001.
- 33. F. Wahaia, I. Kašalynas, L. Minkevičius, C. C. Silva, A. Urbanowicz, and G. Valušis, "Terahertz
- spectroscopy and imaging for gastric cancer diagnosis," *Journal of Spectral Imaging*, vol. 9, no. 1, pp.
- 573 a2, 2020.
- 34. S. Guha and A. R. Lamichhane, "Document classification after dimension reduction through a modified
- Gram-Schmidt process," Wireless Networks and Computational Intelligence, K. R. Venugopal and L.
- M. Patnaik, Eds. Berlin, Germany: Springer, pp. 236–243, 2012.
- 35. X. Zhang, J. Bolton, and P. Gader, "A new learning method for continuous hidden Markov models for
- subsurface landmine detection in ground penetrating radar," *IEEE J. Sel. Topics Appl. Earth Observ.*
- 579 *Remote Sens.*, vol. 7, no. 3, pp. 813–819, 2014.
- 36. Pablo d'Angelo, "Hugin Panorama photo stitcher." http://hugin.sourceforge.net/. Accessed: 7-1-
- 581 2017.